# Interface-Limited Growth of Heterogeneously Nucleated Ice in Supercooled Water

Razvan A. Nistor,[†] Thomas E. Markland,[‡] and B. J. Berne*,[†]

[†]Department of Chemistry, Columbia University, 3000 Broadway, MC 3103, New York, New York 10027, United States
[‡]Department of Chemistry, Stanford University, 333 Campus Drive, Stanford, California 94305, United States

ABSTRACT: Heterogeneous ice growth exhibits a maximum in freezing rate arising from the competition between kinetics and the thermodynamic driving force between the solid and liquid states. Here, we use molecular dynamics simulations to elucidate the atomistic details of this competition, focusing on water properties in the interfacial region along the secondary prismatic direction. The crystal growth velocity is maximized when the efficiency of converting interfacial water molecules to ice, collectively known as the attachment kinetics, is greatest. We find water molecules that contact the intermediate ice layer in concave regions along the atomically roughened surface are more likely to freeze directly. An increased roughening of the solid surface at large undercoolings consequently plays an important limiting role in the rate of ice growth, as water molecules are unable to integrate into increasingly deeper surface pockets. These results provide insight into the molecular mechanisms for self-assembly of solid phases that are important in many biological and atmospheric processes.
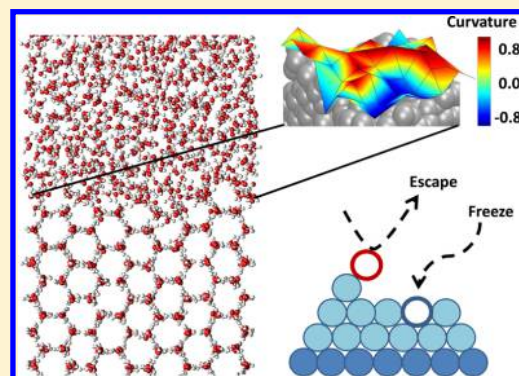
1. INTRODUCTION

Self-assembly of a disordered liquid to an ordered solid is one of the most basic physical processes that occurs in nature.[1,2] Of these processes, the homogeneous and heterogeneous growth of ice from liquid water has attracted considerable attention because of its relevance in atmospheric physics,[3−7] cryobiology,[8,9] and in the antifreeze and food preservation industries.[10−13] However, while the thermodynamics of freezing is largely understood,[14,15] the molecular details of the freezing process are less well-established.

Because of the constantly evolving nature of ice growth, it is difficult to probe the moving solid−liquid interfacial region experimentally at the microscopic level. Measurements have shown the ice−water interface to be on the order of ∼1 nm wide, or three water layers thick, near equilibrium at the melting temperature.[16] Experiments observing dendritic ice growth have measured maximum growth rates on the order of 10 cm/s for the basal plane at temperatures $\Delta T_M = -18$ K below the melting point.[17−19] Experimental deviations of growth rates from theoretical predictions[20] were suggested to be due to an unaccounted-for competition between collective molecular attachment (freezing) and detachment (melting) processes near the solid surface.[20−25]

Molecular dynamics (MD) simulations have proved a useful tool for probing more directly the microscopic properties of the (moving) solid−liquid interface.[26−43] These studies have also shown the interfacial region is about three water layers wide and consists of a slushy mix of ice and liquid features whose dynamical properties are greatly arrested compared to the bulk liquid.[30,33] Ice growth rates were shown to reach a maximum

deep within the supercooled regime, initially increasing as the temperature was lowered below the melting point but then decreasing upon further undercooling below a characteristic temperature.[37,42,44] Ideally, one would like to establish how the structure, shape, dynamics, and molecular attachment rates at the ice surface change with external conditions near this crossover point. If the self-assembly mechanism is a competition between the rates of attachment and detachment at the liquid−solid contact, what microscopic properties at the interface favor molecular retention or loss? Furthermore, what microscopic properties explain why the freezing rate reaches a maximum in the supercooled regime?

Here, we use molecular dynamics simulations to investigate how temperature affects the attachment kinetics of water to the secondary prismatic face of ice I_h. We find the temperature dependence of the ice growth rate reaches a maximum when the microscopic efficiency of converting interfacial water to ice is maximum. This efficiency is limited at higher temperatures because of repeated melting and surface migration[45] events across the interfacial regions. At lower temperatures, the interplay between the roughening of the ice surface and increased tetrahedrality of the liquid[42] play important limiting roles. We find molecules that make contact with the intermediate ice layer in concave regions are more likely to freeze directly. Molecules that make contact with regions of higher curvature tend to escape back into the liquid.

Consequently, water molecules are unable to rearrange and fit into increasingly deeper surface pockets at very low temperatures. Our results highlight the important role played by interfacial water properties in determining the rate of heterogeneous ice growth at increasingly larger undercoolings.

2. SIMULATION DETAILS

Molecular dynamics simulations of the TIP4P/2005 water model[46] were performed using the GROMACS[47] package on the ice–liquid system shown in Figure 1a under isobaric–
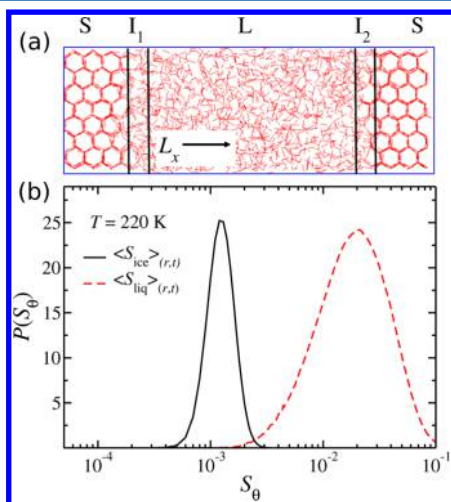
Figure 1. (a) Initial configuration used in the simulations with schematic outlines of the two interfacial regions (I_1, I_2) separating the solid (S) and liquid (L) phases. Ice grows along the L_x-direction. (b) Tetrahedral order parameter distributions where angle brackets $\langle S \rangle_{(r,t)}$ denote both spatial averaging over several configurations of the trajectory, as well as time-based (exponential) smoothing of the resultant instantaneous order parameters for each molecule in separate bulk ice and liquid simulations. Overlap between ice and liquid distributions is significantly reduced using this scheme. The ice distribution is normalized by 1/45 to make the y-axis scale more tractable for viewing.

isothermal conditions. Periodic boundary conditions were employed with the long-range electrostatics treated using particle-mesh Ewald summation.[48] The pressure was kept at 1 bar using an anisotropic Parrinello–Rahman[49] barostat with a time constant of 10 ps. Constant temperature conditions were imposed using a Langevin thermostat with a time constant of 4.0 ps, which quickly removes latent heat from the system.[37,44] Thermostat couplings from 0.1 to 100.0 ps did not affect the observed freezing rates at 240 K within statistical error.

Water intermolecular interactions were modeled using the fully atomistic TIP4P/2005 potential. This model was chosen because it has been shown to accurately reproduce the high-density phase diagram of water and ice[46] as well as the dynamics of water in the supercooled regime.[50] The melting temperature of the model is 250 K,[51] which is considerably more accurate compared with other simple point charge water potentials given the other advantages of this model. Freezing rates obtained with the model are also close to experimentally observed values.[37]

The initial ice structure was prepared according to the Bernal–Fowler rules[52] and brought in contact with an amorphous water configuration approximately three times the thickness of the ice region. The secondary prismatic plane of ice

was chosen to contact the water region because it is the fastest-growing face of ice.[37] The resulting configuration consisted of a sheet of ice (S) and bulk liquid (L) separated by two ice–liquid interfacial regions (I_1, I_2) shown schematically by the vertical lines in Figure 1a. Ice growth was monitored perpendicular to the interface along the L_x direction. Two system sizes were used to assess finite size effects. Ten trajectories at each temperature were performed using a *small* simulation cell containing 2696 water molecules with approximate dimensions $9.1 \times 3.1 \times 2.9$ nm^3. Additionally, three trajectories were performed at each temperature using a *large* simulation cell, which had nine times the cross-sectional surface area of the small system and contained 24 264 water molecules. Data was gathered only until each trajectory was 60% frozen. This ensured that the close proximity of the two interfacial regions in the simulation cell did not affect the analysis at longer times.

3. INTERFACE IDENTIFICATION

We developed a robust scheme for classifying the evolving ice, liquid, and interfacial regions throughout the freezing process. This classification was accomplished by employing a suitable order parameter to distinguish between local ice- and liquidlike structures. Then profile functions of this order parameter were used to identify the instantaneous interface as described below.

3.1. Instantaneous Molecule Classification. We used a local tetrahedral order parameter to classify whether the local structure about a water molecule was ice- or liquidlike[53]

$$S_\theta = \frac{3}{32} \sum_{j=1}^{3} \sum_{k=j+1}^{4} \left(\cos \theta_{jk} + \frac{1}{3} \right)^2 \tag{1}$$

where the summations extended over all hydrogen bond angles θ_{jk} defined by the nearest four neighboring oxygen atoms around a given molecule. To enhance our ability to distinguish between ice- and liquidlike distributions (which can overlap up to 20% at low temperatures), we used a combination of position averaging and exponential time smoothing of the trajectories as described in Appendix A. A water molecule was labeled as icelike when its enhanced order parameter $\langle S_\theta \rangle_{(r,t)}$ was less than a carefully selected threshold criteria S_{tol}. Using the smoothing procedure, near perfect separation between ice and liquid configurations can be obtained with less than 4% overlap between bulk ice and bulk liquid distributions at 220 K, as shown in Figure 1b. The critical threshold value were chosen to be $S_{tol} = 0.002$ for 220 K and $S_{tol} = 0.005$ for all other temperatures. At 300 K, no water molecules were misclassified as icelike in simulations of the bulk liquid. All other observables were calculated from the raw unaveraged trajectories.

3.2. Instantaneous Interface Classification. The instantaneous positions of the interfacial regions were identified from profile functions of the tetrahedral order parameter $\langle S_\theta \rangle_{(r,t)}$ projected along the direction of ice growth. This approach is similar to methods used in previous studies to define the extent of the interfacial region.[26,30,54] Here, we track two interface boundaries as shown in Figure 2a: the solid interface (SI) and the liquid interface (LI). These dividing surfaces (dashed vertical lines in the figure) were identified using the procedure described in Appendix B.

Figure 2b shows the projected density along the scaled simulation box for a typical trajectory at 220 K obtained using this scheme. From these boundary lines, the widths of the interfacial regions (I_1, I_2) and the thicknesses of the ice (S) and liquid (L) regions can be monitored as freezing occurs, as
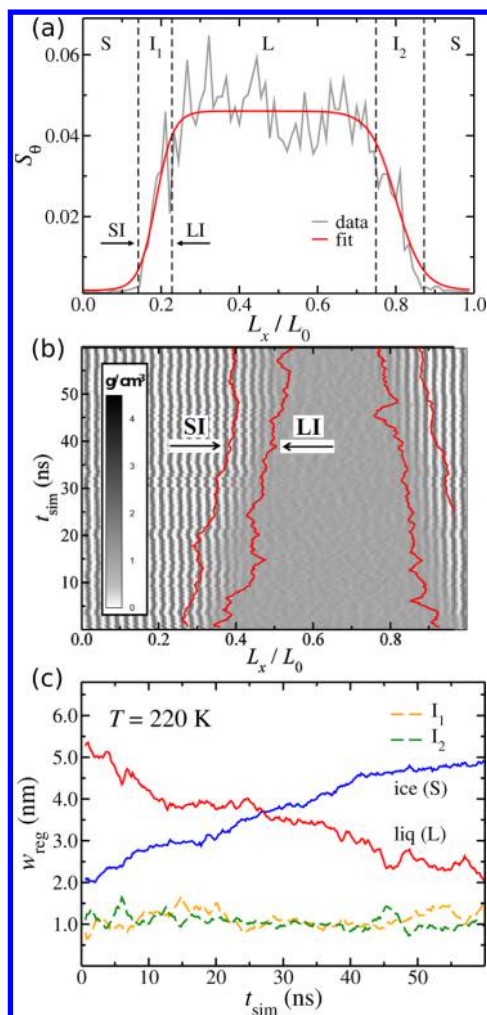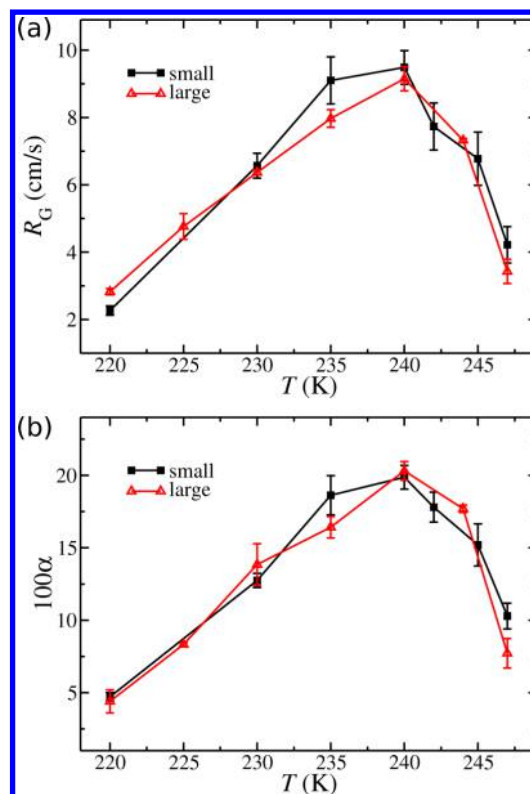
Figure 2. (a) Tetrahedral order parameter binned along direction of ice growth and resultant profile function used to identify the solid interface (SI) and liquid interface (LI) dividing surfaces. (b) Contour map of the density profile evolving during a typical trajectory with the solid lines giving the instantaneous interfacial boundaries (SI and LI) for each interfacial region. (c) Average resultant thicknesses of the ice and liquid and the widths w_{reg} of the interfacial regions (I_1, I_2).

Figure 3. (a) Average crystal growth velocities R_G for the secondary prismatic face of ice I_h for the two system sizes. (b) The retention probability α defining the system efficiency of converting liquid water molecules to ice.

shown in Figure 2c. Importantly, the interfacial widths remain roughly constant throughout the simulation and are on the order of ~1 nm, or approximately three water layers, consistent with experimental measurements[16] and other MD studies.[30,38,43,54]

Because ice growth does not proceed on a layer-by-layer basis along the prismatic directions,[28,33,39] we modeled the rough SI and LI surfaces by dividing the cross-sectional area of the simulation box into a 2D array of fibers extending the entire length of the system along the direction of ice growth. Each square fiber was defined by a feature size of $d_f = 0.6$ nm sides. The envelope functions, and subsequently the positions of the SI and LI boundaries, were formed separately in each fiber.

4. RESULTS AND DISCUSSION

4.1. Growth Rate Maximum. The measured ice growth rates R_G along the secondary prismatic direction for different temperatures are shown in Figure 3a. The growth rate profile reaches a maximum of 9.6 ± 0.5 cm/s at 240 K ($\Delta T_M = -10$ K), in good agreement with previous results using this water

model.[41] Experimental studies of the growth of ice dendrites report growth velocities of 10−12 cm/s for the fastest-growing ice faces at temperatures $\Delta T_M = -18$ K below the melting point.[17,55]

The maximum in the growth rate in Figure 3a is characteristic of a crossover from thermodynamically driven to kinetic-limited crystal growth.[1,37,42,44] From 247 to 240 K, the rate of crystal growth increases by a factor of ~2 as the chemical potential difference between the liquid and solid phases increases (i.e., $\mu_L - \mu_S > 0$) and ice becomes thermodynamically more favorable.[15] Below 240 K, the growth rate progressively decreases and at 220 K is a factor of ~5 smaller than the maximum. This decrease is described as arising from increasing kinetic barriers governing activated processes such as diffusion, which become rate-limiting below 240 K.[1,37] We note the lowest temperature, 220 K, is below where the peak in the isobaric heat capacity occurs for this water model (~225 K, which signifies the onset of water's so-called no-man's land)[56−59] and was included to see if the scaling of the growth process continues as the system enters this deeply cooled regime.

To assess the efficiency with which water molecules in the interfacial regions are incorporated into the ice phase at the varying temperatures, we consider the interfacial retention probability α

$$\alpha = \frac{\Phi_F}{\Phi_F + \Phi_E} \qquad (2)$$

where Φ_F is the flux (number of molecules per square nanometer per nanosecond) of liquid molecules that

irreversibly freeze to the solid surface and Φ_E is the flux of liquid molecules that enter the interfacial region but later escape to the liquid without freezing. Written in this way, α is the liquid-to-ice conversion efficiency of the system, or the percentage of water molecules that freeze from the total number of water molecules that cross into the interfacial regions (I_1 and I_2) from the liquid.

The temperature dependence of the retention probability α in Figure 3b follows the same trend observed in the growth rate profile, exhibiting a maximum at 240 K and minima at the lowest and highest temperatures 220 and 247 K for both system sizes studied. This temperature dependence is intuitively expected because the crystal growth velocity is microscopically determined by the rates which molecules become incorporated into the solid surface. Crystal growth will be limited if the conversion of liquid molecules to ice is low, as is the case at 220 and 247 K in Figure 3b.

The individual contributions to the retention probability in Figure 4 allow the origins of the freezing efficiency to be assessed. As can be seen from Figure 4a, the flux of molecules that irreversibly freeze Φ_F increases by nearly a factor of 2 as the temperature is lowered from 247−240 K and ice becomes thermodynamically more favorable. There are fewer irreversible freeze events at 247 K because of an increased propensity to melt, or to detach from the icelike layers near the solid surface (see next paragraph), which is intuitively expected near the melting point. Below 240 K, however, Φ_F begins to decrease significantly from its maximum value, by up to a factor of ∼4 at 220 K (a similar change in freezing rate is observed in Figure 3a). While the increased tetrahedrality of the liquid[42] and corresponding slow-down in water dynamics[44] are expected to contribute to the observed decrease in freeze events, we examine further how changes in the interfacial structure can also play a limiting role in the attachment kinetics at low temperatures.

The escape flux of molecules that enter the interfacial region but return to the liquid is shown in Figure 4b. The nonmonotonic behavior shows that the number of escape events is (somewhat unintuitively) greater at both 220 and 247 K. An increased propensity to detach from the ice surface (or icelike layers near the ice surface) plays an increasingly greater role in the escape flux as the temperature increases. Figure 4c shows how the flux Φ_M of frozen molecules that detach from the ice and icelike planes near the solid surface, i.e., melt events, increases with temperature and proximity to the liquid region (dashed lines), as is intuitively expected. At temperatures below 240 K, however, increasing values for Φ_E are more puzzling. This greater propensity to return to the liquid will be attributed to a roughening of the intermediate ice layers, as will be discussed below.

The microscopic population analysis shows that although the system has similarly low retention probability and ice growth rates at 220 and 247 K, the reasons for the limited growth velocities are quite different. At high temperatures, the growth rate is limited because of an increased melting propensity. At low temperature, the growth rate is limited by a sharp decrease in the number of direct freezing events because of an inability to convert interfacial water molecules into ice before these molecules also escape back to the liquid. In the following sections, we analyze how the microscopic dynamics and interface topology contribute to these observations.

4.2. Effects of Interface Topology. It is constructive to analyze the collective freezing and melting events at the solid
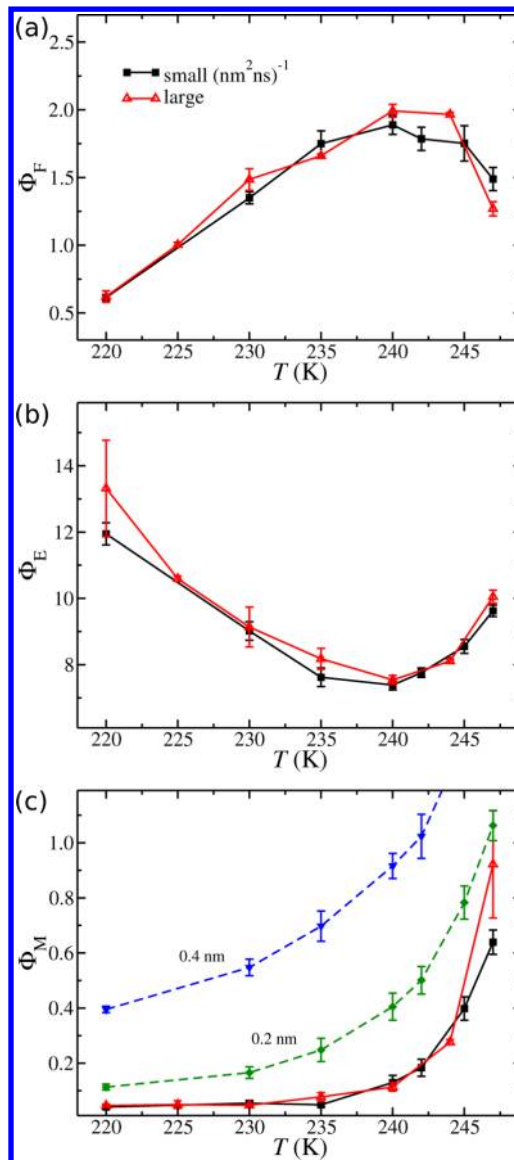
Figure 4. (a) Flux Φ_F of molecules that irreversibly freeze to the solid phase. (b) Flux Φ_E of molecules that cross into the interfacial regions but later escape to the liquid without contacting the ice surface. (c) Flux Φ_M of molecules that escape to the liquid (melt) from the ice surface (solid lines) and icelike planes progressively farther into the interfacial region (dashed lines).

interface (SI) guided by a simple model. As discussed in Instantaneous Interface Classification, we approximate the roughening of the interfacial dividing surfaces by fitting envelope functions of $\langle S_\theta \rangle_{(r,t)}$ in a series of discretized rectangular fibers extending the length of the simulation box. If the fluctuating position of the SI in each fiber is treated as a biased random walker, where a step forward represents a freezing event and a step backward represents a melting event, and where the random walk is biased by the degree of undercooling, then ensemble averages over all the fibers derived using the moment-generating function for continuous walks will satisfy[60]

$$\langle \delta x(\tau) \rangle = \langle x_i(t_0 + \tau) - x_i(t_0) \rangle = (k_f - k_b)a\tau \qquad (3)$$

and

$$\langle \delta x^2(\tau) \rangle = \langle \delta x(\tau)^2 \rangle - \langle \delta x(\tau) \rangle^2 = (k_{\mathrm{f}} + k_{\mathrm{b}}) a^2 \tau \qquad (4)$$

where $x_i(\tau)$ is the position of the ith cell or fiber at time τ; $k_{\mathrm{f}}a$ and $k_{\mathrm{b}}a$ are the forward (freezing) and backward (melting) rates, respectively; and a is the average measured step size. Equation 3 gives the growth rate (or velocity) as $R_{\mathrm{G}} = (k_{\mathrm{f}} - k_{\mathrm{b}})a$. Equation 4 is a measure of the spread of the random walker trajectories. Using these relations, the forward and backward rates can be extracted for each temperature.

Figure 5a shows the nonmonotonic temperature dependence of the forward (k_{f}) and backward (k_{b}) rates for the two system sizes using a feature size of $d_{\mathrm{f}} = 0.6$ nm for the square fibers defining the discretized random walkers. We have separately verified that the trends are qualitatively reproduced using (1)
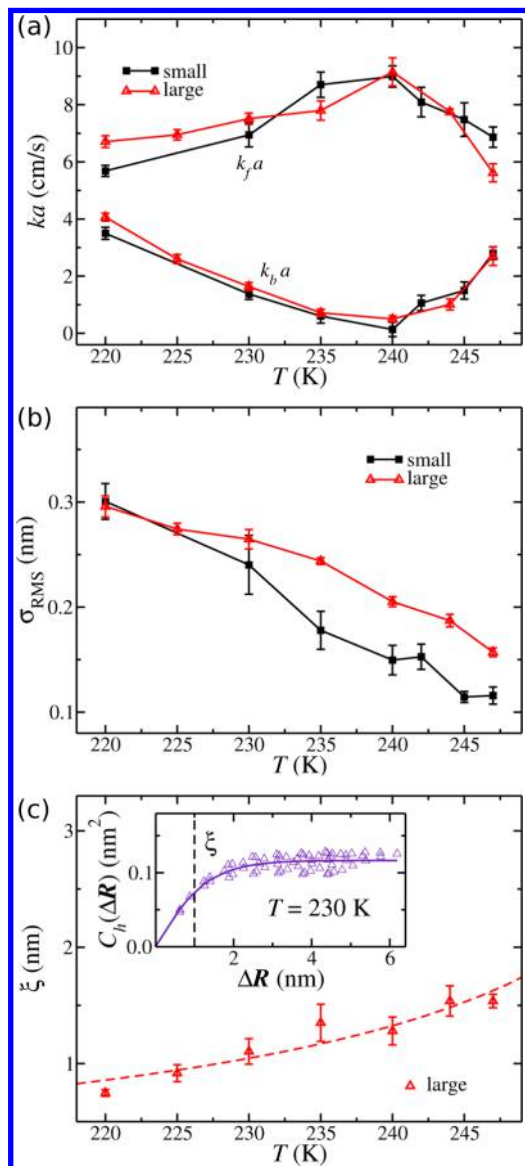
Figure 5. (a) Forward (k_{f}) and backward (k_{b}) rates representing freezing and melting processes of the solid interface for the two different sized systems. Results are multiplied by the measured average step size $a = 0.23$ nm, which roughly equals the spacing between successive ice planes. (b) Root-mean-squared deviation of the discretized roughened ice surface σ_{RMS}. (c) Spatial correlation lengths ξ for the large systems extracted by fitting the height difference correlation function shown in the inset as an example at $T = 230$ K.

thicker fibers up to $d_{\mathrm{f}} = 1.0$ nm, (2) interfacial profile functions constructed from the total density ρ,[30] and (3) trajectories generated using the standard TIP4P water model[61] (at relative undercoolings).

The forward rate k_{f} increases by a factor of ∼1.3 from 247−240 K, and progressively decreases by a factor of ∼1.5 from 240−220 K. The backward rate shows a stronger non-monotonic temperature dependence: decreasing by a factor of ∼5 from 247 K to the minimum at 240 K and increasing by roughly the same factor upon further cooling to 220 K. The nonmonotonic behavior in Figure 5a shows that the difference between forward and backward processes, and consequently the growth rate $R_{\mathrm{G}} = (k_{\mathrm{f}} - k_{\mathrm{b}})a$, is greatest at 240 K and lowest at both 220 and 247 K. While low thermodynamic driving force and increased melting propensity can intuitively describe the small difference in $(k_{\mathrm{f}} - k_{\mathrm{b}})a$ at 247 K (see also Figure 4a,b), it is instructive to analyze how changes in interfacial structure coupled with arrested water dynamics[44] and increased tetrahedrality of the liquid[42] can limit the attachment kinetics that microscopically underpin the forward and backward rates at low temperatures.

The microscopic features of the interfacial regions are intricately linked to nonmonotonic temperature dependence of the forward and backward processes at increasingly lower temperatures. Notably, the structural characteristics of the solid−liquid interface scale differently than in solid−vapor systems. Figure 5b shows the root-mean-squared (RMS) deviation of the discretized fibers used to define the instantaneously roughened solid interface for all temperatures. The figure shows that the dividing surface becomes rougher as the temperature is lowered, consistent with previous simulations,[38] but opposite to what is observed at the ice−vapor interface.[14,62] The RMS deviation is slightly larger than 0.3 nm at the coldest temperatures, corresponding approximately to an extra ice layer, or half a hexagon as viewed from the basal direction. The larger systems show higher RMS deviations at higher temperatures, which is a notable finite size effect.

Small systems in particular can lead to overestimated growth kinetics.[37] To understand how this arises, Figure 5c shows the roughness correlation length ξ extracted from the height difference spatial correlation function for the large systems[63,64]

$$C_h(\Delta \mathbf{R}) = \langle |h(\mathbf{r}) - h(\mathbf{r}')|^2 \rangle \qquad (5)$$

where $h(\mathbf{r})$ is the height of the discretized fiber (in this case, its extent along the x-direction) at position $\mathbf{r}$ along the cross-sectional area of the roughened surface and $\Delta \mathbf{R} = \mathbf{r} - \mathbf{r}'$. The roughness correlation length was extracted by fitting the function $C_h(\Delta \mathbf{R})$ to the form[64]

$$C_h(\Delta \mathbf{R}) = 2\sigma^2 \{ 1 - \exp[-(\Delta \mathbf{R}/\xi)^{2P}] \} \qquad (6)$$

where σ is the standard deviation in heights, ξ the correlation length, and P a roughness exponent, typically between 0.5 and 0.6 for the large systems. The temperature dependence of ξ can be fitted to the Kosterlitz−Thouless scaling relation (dashed line), which increases exponentially and diverges at the roughening transition temperature near the melting point.[65] At 247 K, the roughness correlation length is nearly 1.6 nm, almost half the size of the large system simulation cell. These data indicate that finite size effects will become prevalent if long-wavelength capillary waves driving the roughening transition are damped out because of small simulation cells. Higher observed growth rates in sufficiently small systems

could result because of the appearance of defected surface motifs that aid molecular rearrangement near the solid surface.[63,66]

The increase in the roughness correlation length with temperature in Figure 5c shows structural features are more correlated at higher temperatures. Consequently, the solid interface appears smoother, with a smaller RMS deviation in the height profiles of the discretized fibers. At lower temperatures, structural correlations occur over shorter length scales and the ice surface becomes rougher.

To gain insight into which properties of the roughened interface inhibit molecular retention at low temperatures, we track where incoming molecules contact the intermediate ice layer (IIL), which is typically composed of a few roughened water layers above the ice boundary as described in Appendix A. We divide the flux of these incoming molecules into molecules that freeze and molecules that escape back to the liquid without being incorporated in the solid phase. We measure the average distance d of a water molecule to this IIL and the curvature κ of the roughened surface at the contact point. Contact is defined by the formation of hydrogen bonds between the incoming water molecule and molecules that are part of the IIL. The mean curvature κ at each point of the atomistically rough intermediate ice surface was calculated from the average of the principal curvatures, $\kappa = 1/2(\kappa_{min} + \kappa_{max})$, where κ_{min} and κ_{max} are the eigenvalues of the shape operator representing the minimum and maximum degree of deflection of a surface at a given point.[67]

As an example, Figure 6a shows the curvature distributions for the freezing and escaping populations averaged over all trajectories at 230 K. Molecules that directly freeze tend to dock in concave valleys, or regions of negative (or near zero) mean curvature on the roughened intermediate ice surface. Conversely, molecules that escape back into the liquid tend to bind to peaks, or regions of high mean curvature farther away from the solid interface. Particles subsequently have a greater propensity to escape from convex surfaces than from concave surfaces of ice, as seems to be the case for liquid−vapor interfaces as well (see refs 63 and 68.).

Figure 6b measures the degree of overlap between the freeze and escape distributions for both observables, quantified by taking differences in the mean values: $\Delta\kappa = \langle\kappa_{escape}\rangle - \langle\kappa_{freeze}\rangle$ and $\Delta d = \langle d_{escape}\rangle - \langle d_{freeze}\rangle$. The differences in both $\Delta\kappa$ and Δd decrease as the temperature approaches the melting point, where the solid surface is much flatter. Analogously, there are fewer peaks and valleys for the smoother interfaces at higher temperatures and less of a docking preference between freeze and escape populations. At large undercoolings, however, the separation between distributions is larger, indicating that escape events preferentially bind to regions of higher curvature. These roughened structural features may develop in order to expose the more stable prismatic face to the liquid contact.[32,69] However, surface roughening has been noted to appear on the prismatic and basal faces of ice as well.[39]

To asses how the roughened structural features of the ice surface impact the growth kinetics, Figure 6c shows Pearson's statistical correlation coefficient g_{corr} between the instantaneous growth rates R_G and surface roughness σ_{RMS} for the large systems. Instantaneous growth rates were obtained from 2.0 ns moving windows centered at each frame of the trajectories. The coefficient is −1.0 when growth rates are completely anticorrelated with surface roughness. When g_{corr} is 0.0, the two measures are uncorrelated. As can be seen in the figure,
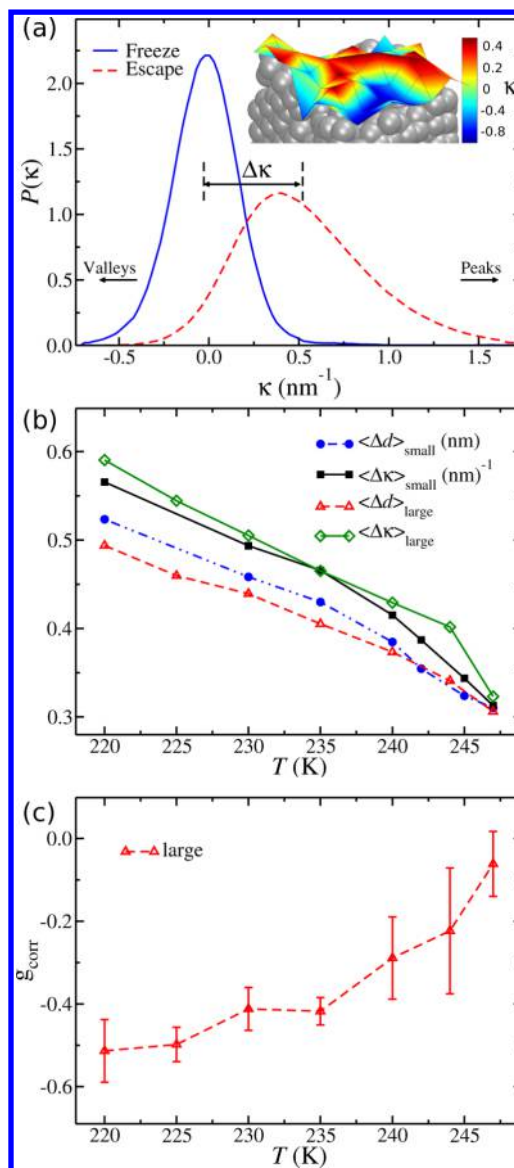
Figure 6. (a) Mean curvature distributions κ of freeze and escape populations at $T = 230$ K. The inset shows a colormap of the resulting curvature values atop an instantaneous configuration of the intermediate ice layer. (b) Differences between freeze and escape distributions for the two measures, $\langle\Delta d\rangle$ and $\langle\Delta\kappa\rangle$, for the two system sizes. (c) Statistical correlation g_{corr} between low growth rate and high surface roughness for the large systems.

g_{corr} approaches 0.0 at high temperatures and -0.51 ± 0.08 as the temperature is lowered to 220 K. Consequently, *low* growth rates are increasingly associated with *high* surface roughness below the temperature of maximum crystallization.

5. SUMMARY AND CONCLUSIONS

Using molecular dynamics simulations, we have identified structural features of the ice−liquid interface along the secondary prismatic direction that affect crystal growth velocities in the supercooled regime. Near the melting point, the freezing rate is limited by surface depletion events, as molecules detach from the ice and migrate back to the liquid. At much lower temperatures, the topology of the roughened intermediate ice layer plays an important limiting role hindering ice growth. The decrease in the interfacial retention probability

at low temperatures is due to the appearance of high-curvature structural motifs. Along with the increased tetrahedrality of the liquid,[42] these roughened structural profiles limit the crystal growth velocities at larger undercoolings, as the liquid is unable to adjust to the required surface geometry.

At the temperature of maximum crystallization, the efficiency of converting interfacial water to ice is maximized. The rates between competing attachment and detachment reactions in the interfacial region is greatest at this temperature. Notably, molecular detachment rates leading to surface melting are minimized when the crystallization rate is maximized. The liquid is best able to adjust and fill surface pockets at the temperature of maximum growth.

These insights into the molecular scale rate-limiting processes for heterogeneous ice nucleation should prove useful in analyzing how other perturbations, such as the presence of solutes, affect the interfacial region and freezing rates. Such an understanding is vital for unraveling the ice growth inhibition mechanisms of antifreeze proteins in biological systems and for industrial cryogenics applications.

■ APPENDIX

A. Ice−Water Selectivity

In order to enhance the selectivity between ice- and liquidlike local configurations using the tetrahedral order parameter in eq 1, the atomic positions of the trajectories were first averaged over 5 ps windows to reduce thermal and librational noise in the oxygen atom positions. This time is shorter than the ∼10 ps characteristic water reorientation time for this water model at 250 K,[50] which is a higher than any temperature used here and so is much shorter than the characteristic time in which a molecule can interconvert between ice and water in our trajectories. These averaged positions were then used to evaluate the tetrahedral order parameter using eq 1 for each water molecule.

The order parameter history of each water molecule from the position-averaged trajectories was then exponentially time-smoothed using $\langle S_\theta \rangle_{(r,t)} = \alpha \langle S_\theta \rangle_{(r)} + (1 - \alpha)\langle S_\theta \rangle_{(r,t-1)}$, where $\langle S_\theta \rangle_r$ is the instantaneous position-averaged order parameter of a given molecule at time t, $\langle S_\theta \rangle_{(r,t-1)}$ the smoothed order parameter of the previous time step $t - 1$, and α the smoothing parameter. We found $\alpha \sim 0.3$ gave adequate separation between bulk ice and liquid distributions at low temperatures. This time-based smoothing was used to inhibit instantaneous tetrahedral configurations from contributing to the analysis, which may spontaneously occur even at high temperatures.

Molecules within the interfacial regions whose order parameter $\langle S_\theta \rangle_{(r,t)}$ was greater than the ice threshold criteria S_{tol} but less than 75% of the liquid value at the given temperature were labeled as intermediate ice.[42] A molecule retained its ice, liquid, or intermediate ice label for the duration of the 5 ps position-averaging window. These labels were used only for population analysis.

B. Interface Identification

In order to identify the (moving) positions of the solid and liquid interface dividing surfaces, the order parameter $\langle S_\theta \rangle_{(r,t)}$ was binned across the simulation cell as shown in Figure 2a. The resulting distributions were fitted to profile functions of the form $f(x) = A[\tanh(x - C/B) - \tanh(x - D/E)]$, where $\{A,B,C,D,E\}$ were the fit parameters. The roots of the fourth derivative of this function lie close to the positions of the shoulders of the profile and were used here to define the

locations of the SI and LI dividing surfaces as shown by the dashed vertical lines in Figure 2a.

The distributions were accrued over 200 ps time windows. This sampling corresponded to roughly one-tenth the time it took the solid interface to pass through the next layer of ice in the fastest-growing trajectories. The positions of the SI boundaries were aligned with the nearest ice plane at each time step because the lower shoulders of the fitted profile function were not necessarily concomitant with the outermost ice layer. Once the interfacial boundaries were established, molecules could be identified as being in the solid (S), liquid (L), or in one of the two interfacial (I_1, I_2) regions at any given time in the trajectory. To remove rapid recrossing events across the boundaries, a molecule was required to reside a minimum of 200 ps in a region before it counted towards the population statistics. Molecular configurations and surfaces were rendered using MATLAB and the Visual Molecular Dynamics (VMD) package.[70,71]

■ AUTHOR INFORMATION

Corresponding Author

*E-mail: bb8@columbia.edu.

Notes

The authors declare no competing financial interest.

■ ACKNOWLEDGMENTS

■ REFERENCES

(1) Kirkpatrick, R. J. Crystal Growth from the Melt: A Review. *Am. Mineral.* **1975**, *60*, 798−814.

(2) Levi, A. C.; Kotrla, M. Theory and Simulation of Crystal Growth. *J. Phys.: Condens. Matter.* **1997**, *9*, 299−344.

(3) Petrenko, V. F.; Whitworth, R. W. *Physics of Ice*; University Press: Oxford, U.K., 2002.

(4) Koop, T.; Luo, B.; Tsias, A.; Peter, T. Water Activity as the Determinant for Homogeneous Ice Nucleation in Aqueous Solutions. *Nature* **2000**, *406*, 611−614.

(5) Murray, B. J.; Knopf, D. A.; Bertram, A. K. The Formation of Cubic Ice Under Conditions Relevant to Earth's Atmosphere. *Nature* **2005**, *434*, 202−205.

(6) Murphy, D. M.; Koop, T. Review of the Vapour Pressures of Ice and Supercooled Water for Atmospheric Applications. *Q. J. R. Meteorol. Soc.* **2005**, *131*, 1539−1565.

(7) Cantrell, W.; Heymsfield, A. Production of Ice in Tropospheric Clouds: A Review. *Bull. Am. Meteorol. Soc.* **2005**, *86*, 795−807.

(8) Mazur, P. Kinetics of Water Loss from Cells at Subzero Temperatures and the Likelihood of Intracellular Freezing. *J. Gen. Physiol.* **1963**, *47*, 347−369.

(9) Mazur, P. Cryobiology: The Freezing of Biological Systems. *Science* **1970**, *168*, 939−949.

(10) Griffith, M.; Ewart, K. V. Antifreeze Proteins and their Potential Use in Frozen Foods. *Biotech. Adv.* **1995**, *13*, 375−402.

(11) Feeney, R. E.; Yeh, Y. Antifreeze Proteins: Current Status and Possible Food Uses. *Trends Food Sci. Technol.* **1998**, *9*, 102−106.

(12) Carvajal-Rondanelli, P. A.; Marshall, S. H.; Guzman, F. Antifreeze Glycoprotein Agents: Structural Requirements for Activity. *J. Sci. Food Agric.* **2011**, *91*, 2507−2510.

(13) Hassas-Roudsari, M.; Goff, H. D. Ice Structuring Proteins from Plants: Mechanism of Action and Food Application. *Food Res. Int.* **2012**, *46*, 425−436.

(14) Libbrecht, K. G. The Physics of Snow Crystals. *Rep. Prog. Phys.* **2005**, *68*, 855.

(15) Bartels-Rausch, T.; Bergeron, V.; Cartwright, J. H. E.; Escribano, R.; Finney, J. L.; Grothe, H.; Gutiérrez, P. J.; Haapala, J.; Kuhs, W. F.; Pettersson, J. B. C.; et al. Ice Structures, Patterns, and Processes: A View Across the Icefields. *Rev. Mod. Phys.* **2012**, *84*, 885−944.

(16) Beaglehole, D.; Wilson, P. Thickness and Anisotropy of the Ice−Water Interface. *J. Phys. Chem.* **1993**, *97*, 11053−11055.

(17) Pruppacher, H. R. Interpretation of Experimentally Determined Growth Rates of Ice Crystals in Supercooled Water. *J. Chem. Phys.* **1967**, *47*, 1807−1813.

(18) Langer, J. S.; Sekerka, R. F.; Fujioka, T. Evidence for a Universal Law of Dendritic Growth Rates. *J. Cryst. Growth* **1978**, *44*, 414−418.

(19) Furukawa, Y.; Shimada, W. Three Dimensional Pattern Formation During Growth of Ice Dentrites - Its Relation to Universal Law of Dendritic Growth. *J. Cryst. Growth* **1993**, *128*, 238−239.

(20) Shibkov, A.; Zheltov, M.; Korolev, A.; Kazakov, A.; Leonov, A. Crossover from Diffusion-Limited to Kinetics-Limited Growth of Ice Crystals. *J. Cryst. Growth* **2005**, *285*, 215−227.

(21) Wilson, H. A. On the Velocity of Solidification and the Viscosity of Supercooled Liquids. *Philos. Mag.* **1900**, *50*, 238−250.

(22) Frenkel, J. Note on the Relation Between the Speed of Crystallization and Viscosity. *Phys. Z. Sowjetunion* **1932**, *1*, 498.

(23) Kolmogorov, A. N. A Statistical Theory for the Recrystallization of Metals. *Bull. Acad. Sci. URSS, Cl. Sci. Math. Nat.* **1937**, *3*, 355−359.

(24) Johnsson, W. A.; Mehl, R. F. Reaction Kinetics in Processes of Nucleation and Growth. *Trans. Am. Inst. Min., Metall. Pet. Eng.* **1940**, *135*, 416−442.

(25) Avrami, M. Kinetics of Phase Change. II Transformation-Time Relations for Random Distribution of Nuclei. *J. Chem. Phys.* **1940**, *8*, 212−240.

(26) Karim, O. A.; Haymet, A. D. J. The Ice/Water Interface. *Chem. Phys. Lett.* **1987**, *138*, 531−534.

(27) Karim, O. A.; Haymet, A. D. J. The Ice/Water Interface: A Molecular Dynamics Study. *J. Chem. Phys.* **1988**, *89*, 6889−6896.

(28) Nada, H.; Furukawa, Y. Anisotropic Properties of Ice/Water Interface: A Molecular Dynamics Study. *Jpn. J. Appl. Phys.* **1995**, *34*, 583−588.

(29) Baéz, L. A.; Clancy, P. Phase Equilibria in Extended Simple Point Charge Ice-Water Systems. *J. Chem. Phys.* **1995**, *103*, 9744−9755.

(30) Hayward, J. A.; Haymet, A. D. J. The Ice/Water Interface: Molecular Dynamics Simulations of the Basal, Prism, $\{20\bar{2}1\}$, and $\{2\bar{1}\bar{1}0\}$ Interfaces of Ice Ih. *J. Chem. Phys.* **2001**, *114*, 3713−3726.

(31) Hayward, J. A.; Haymet, A. D. J. The Ice/Water Interface: Orientational Order Parameters for the Basal, Prism, $\{20\bar{2}1\}$, and $\{2\bar{1}\bar{1}0\}$ Interfaces of Ice Ih. *Phys. Chem. Chem. Phys.* **2002**, *4*, 3712−3719.

(32) Nada, H.; Furukawa, Y. Anisotropy in Growth Kinetics at Interfaces Between Proton-Disordered Hexagonal Ice and Water: A Molecular Dynamics Study Using the Six-Site Model of H_2O. *J. Cryst. Growth* **2005**, *283*, 242−256.

(33) Carignano, M. A.; Shepson, P.; Szleifer, I. Molecular Dynamics Simulations of Ice Growth from Supercooled Water. *Mol. Phys.* **2005**, *103*, 2957−2967.

(34) Kim, J. S.; Yethiraj, A. The Effect of Salt on the Melting of Ice: A Molecular Dynamics Simulation Study. *J. Chem. Phys.* **2008**, *129*, 124504.

(35) Kim, J. S.; Damodaran, S.; Yethiraj, A. Retardation of Ice Crystallization by Short Peptides. *J. Phys. Chem. A* **2009**, *113*, 4403−4407.

(36) Pirzadeh, P.; Kusalik, P. G. On Understanding Stacking Fault Formation in Ice. *J. Am. Chem. Soc.* **2011**, *133*, 704−707.

(37) Rozmanov, D.; Kusalik, P. G. Temperature Dependence of Crystal Growth of Hexagonal Ice (I_h). *Phys. Chem. Chem. Phys.* **2011**, *13*, 15501−15511.

(38) Pirzadeh, P.; Beaudoin, E. N.; Kusalik, P. G. Interfacial Free Energy: An Entropy Portent to Energy Changes. *Crys. Growth Des.* **2012**, *12*, 124−128.

(39) Seo, M.; Jang, E.; Kim, K.; Choi, S.; Kim, J. S. Understanding Anisotropic Growth Behavior of Hexagonal Ice on a Molecular Scale: A Molecular Dynamics Simulation Study. *J. Chem. Phys.* **2012**, *137*, 154503.

(40) Rozmanov, D.; Kusalik, P. G. Isoconfigurational Molecular Dynamics Study of the Kinetics of Ice Crystal Growth. *Phys. Chem. Chem. Phys.* **2012**, *14*, 13010−13018.

(41) Rozmanov, D.; Kusalik, P. G. Anisotropy in the Crystal Growth of Hexagonal Ice, I_h. *J. Chem. Phys.* **2012**, *137*, 094702.

(42) Moore, E. B.; Molinero, V. Structural Transformation in Supercooled Water Controls the Crystallization Rate of Ice. *Nature* **2011**, *479*, 506−509.

(43) Shepherd, T. D.; Koc, M. A.; Molinero, V. The Quasi-Liquid Layer of Ice under Conditions of Methane Clathrate Formation. *J. Phys. Chem. C* **2012**, *116*, 12172−12180.

(44) Weiss, V. C.; Rullich, M.; Köhler, C.; Frauenheim, T. Kinetic Aspects of the Thermostatted Growth of Ice from Supercooled Water in Simulations. *J. Chem. Phys.* **2011**, *135*, 034701.

(45) Rost, M. J.; Quist, D. A.; Frenken, J. W. M. Grains, Growth, and Grooving. *Phys. Rev. Lett.* **2003**, *91*, 026101.

(46) Abascal, J. L. F.; Vega, C. A General Purpose Model for the Condensed Phases of Water: TIP4P/2005. *J. Chem. Phys.* **2005**, *123*, 234505.

(47) Hess, B.; Kutzner, C.; van der Spoel, D.; Lindahl, E. GROMACS 4: Algorithms for Highly Efficient, Load-Balanced, and Scalable Molecular Simulation. *J. Chem. Theory Comput.* **2008**, *4*, 435−447.

(48) Essmann, U.; Perera, L.; Berkowitz, M. L.; Darden, T.; Lee, H.; Pedersen, L. G. A Smooth Particle Mesh Ewald Method. *J. Chem. Phys.* **1995**, *103*, 8577−8593.

(49) Parrinello, M.; Rahman, A. Polymorphic Transitions in Single Crystals: A New Molecular Dynamics Method. *J. Appl. Phys.* **1981**, *52*, 7182−7190.

(50) Stirnemann, G.; Laage, D. Communication: On the origin of the Non-Arrhenius Behavior in Water Reorientation Dynamics. *J. Chem. Phys.* **2012**, *137*.

(51) Fernández, R. G.; Abascal, J. L. F.; Vega, C. The Melting Point of Ice I_h for Common Water Models Calculated from Direct Coexistence of the Solid-Liquid Interface. *J. Chem. Phys.* **2006**, *124*, 144506.

(52) Bernal, J. D.; Fowler, R. H. A Theory of Water and Ionic Solution, with Particular Reference to Hydrogen and Hydroxyl Ions. *J. Chem. Phys.* **1933**, *1*, 515.

(53) Chau, P.-L.; Hardwick, A. J. A New Order Parameter for Tetrahedral Configurations. *Mol. Phys.* **1998**, *93*, 511−518.

(54) Razul, M. S. G.; Kusalik, P. G. Crystal Growth Investigations of Ice/Water Interfaces from Molecular Dynamics Simulations: Profile Functions and Average Properties. *J. Chem. Phys.* **2011**, *134*, 014710.

(55) Bauerecker, S.; Ulbig, P.; Buch, V.; Vrbka, L.; Jungwirth, P. Monitoring Ice Nucleation in Pure and Salty Water via High-Speed Imaging and Computer Simulations. *J. Phys. Chem. C* **2008**, *112*, 7631−7636.

(56) Mishima, O.; Stanley, H. E. The Relationship Between Liquid, Supercooled and Glassy Water. *Nature* **1998**, *396*, 329−335.

(57) Moore, E. B.; Molinero, V. Ice Crystallization in Water's "No-Man's Land". *J. Chem. Phys.* **2010**, *132*, 244504.

(58) Abascal, J. L. F.; Vega, C. Widom Line and the Liquid-Liquid Critical Point for the TIP4P/2005 Water Model. *J. Chem. Phys.* **2010**, *133*, 234502.

(59) Malaspina, D. C.; di Lorenzo, A. J. B.; Pereyra, R. G.; Szleifer, I.; Carignano, M. A. The Water Supercooled Regime as Described by Four Common Water Models. *J. Chem. Phys.* **2013**, *139*, 024506.

(60) Spitzer, F. *Principles of Random Walk*; Springer-Verlag: New York, 1976.

(61) Jorgensen, W. L.; Chandrasekhar, J.; Madura, J. D.; Impey, R. W.; Klein, M. L. Comparison of Simple Potential Functions for Simulating Liquid Water. *J. Chem. Phys.* **1983**, *79*, 926−935.

(62) Cahn, J. W.; Hilliard, J. E. Free Energy of a Nonuniform System. I. Interfacial Free Energy. *J. Chem. Phys.* **1958**, *28*, 258−257.

(63) Weeks, J. D.; Gilmer, G. H. In *Advances in Chemical Physics*; Prigogine, I., Rice, S. A., Eds.; John Wiley: New York, 1979; Vol. *40*; pp 157−228.

(64) Salditt, T.; Metzger, T. H.; Brandt, C.; Klemradt, U.; Peisl, J. Determination of the Static Scaling Exponent of Self-Affine Interfaces by Nonspecular X-Ray Scattering. *Phys. Rev. B* **1995**, *51*, 5617−5627.

(65) Kosterlitz, J. M.; Thouless, D. J. Ordering, Metastability and Phase Transitions in Two-Dimensional Systems. *J. Phys. C: Solid State Phys.* **1973**, *6*, 1181−1203.

(66) Broughton, J. Q.; Gilmer, G. H. Molecular Dynamics Investigation of the Crystal-Fluid Interface. III. Dynamical Properties of FCC Crystal-Vapor Systems. *J. Chem. Phys.* **1983**, *79*, 5119−5127.

(67) Toponogov, V. A. *Differential Geometry of Curves and Surfaces: A Concise Guide*; Birkhäuser: Boston, MA, 2006; pp 83−86.

(68) Willard, A. P.; Chandler, D. Instantaneous Liquid Interfaces. *J. Phys. Chem. B* **2010**, *114*, 1954−1958.

(69) Pereyra, R. G.; Carignano, M. A. Ice Nanocolumns: A Molecular Dynamics Study. *J. Phys. Chem. C* **2009**, *113*, 12699−12705.

(70) MATLAB, version 7.0.1 (R14SP1); The MathWorks Inc.: Natick, MA, 2005.

(71) Humphrey, W.; Dalke, A.; Schulten, K. VMD - Visual Molecular Dynamics. *J. Mol. Graphics* **1996**, *14*, 33−38.

760

dx.doi.org/10.1021/jp408832b | J. Phys. Chem. B 2014, 118, 752−760